Supporting information

Ni^{2+} mediated the oxidation and aggregation of *o*-phenylenediamine: Enhanced photothermal effect for direct, specific and background-free detection of thiophanate-methyl

Jinju Xu, Ziyi Qin, Chunhui Liao, Tian Lan, and Shuyun Shi*

College of Chemistry and Chemical Engineering, Central South University, Changsha 410083, Hunan, China

*Corresponding author: Tel./fax: +86 731 88879616.

E-mail addresses: shishuyun@126.com, shuyshi@csu.edu.com (S. Shi).

Partial experimental section

Partial results and discussion

Figure number: Figure S1−S15

Table   **number**:   Table   S1−S2

1. Experimental Section

1.1. Reagents and Instruments

1,3,5-benzenetricarboxylic acid (H$_3$BTC, 98%, AR), N,N-dimethylformamide (DMF, 99%, AR), thiophanate-methyl (TM, 99%, AR), glyphosate (98%, AR), dichlorvos (1 mg mL^{-1}, AR), dipterex (1 mg mL^{-1}, AR), naled (1 mg mL^{-1}, AR), carbaryl (1 mg mL^{-1}, AR), parathion (1 mg mL^{-1}, AR), parathion-methyl (MP, 1 mg mL^{-1}, AR), carbendazim (98%, AR), thiram (99%, AR), fipronil (99%, AR), and anhydrous ethanol (AR) were brought from Shanghai Aladdin Bio-Chem Technology Co., Ltd. (Shanghai, China). Tris-(hydroxymethyl)-aminomethane (Tris, AR), o-phenylenediamine (OPD, 98%, AR), NH$_3$·H$_2$O (25%−28%, GR), BaSO$_4$ (99%, AR), Ni(NO$_3$)$_2$·6H$_2$O (99%, AR), Ni(CH$_3$COO)$_2$·4H$_2$O (99.9%, AR), Cu(NO$_3$)$_2$·3H$_2$O (99%, AR), CoCl$_2$·6H$_2$O (99%, AR), FeSO$_4$·7H$_2$O (99%, AR), AgCl (99%, AR), Cr(NO$_3$)$_3$·9H$_2$O (99%, AR), CdCl$_2$·2.5H$_2$O (99%, AR), CsCl (99%, AR), ZnSO$_4$·7H$_2$O (99%, AR), Li$_2$CO$_3$ (99%, AR), CuSO$_4$·5H$_2$O (99%, AR), MnCl$_2$·4H$_2$O (99%, AR), Ce(CH$_3$COO)$_3$ (99%, AR), NaNO$_3$ (99%, AR), Al(NO$_3$)$_3$·9H$_2$O (99%, AR), 2,3,6,7,10,11-hexaaminotriphenylene hexahydrochloride (HATP·6HCl, 95%, GR), acetonitrile (HPLC), formic acid (HPLC), and methanol (HPLC) were supplied by Sinopharm Chemical Reagent Co., Ltd (Beijing, China). Dimethyl sulfoxide (DMSO, 99% AR), NaOH (97%, AR), HCl (36–38%, GR), NaCl (99%, AR), KCl (99%, AR), MgCl$_2$ (98%, AR), CaCl$_2$ (96%, AR), FeCl$_3$ (98%, AR), K$_3$[Fe(CN)$_6$] (99%, AR), and 1,4-benzenedicarboxylic acid (BDC, 99%, AR) were obtained from Shanghai Macklin Biochemical Co., Ltd. (Shanghai, China). Aspartic acid (L-Asp, 99%, BR), glutamic acid (L-Glu, 99%, BR), serine (L-Ser, 99%, BR), and alanine (L-Ala, 99%, BR) were gained from Shanghai Yuanye Bio-Technology Co., Ltd. (Shanghai, China). Ultrapure water (18.25 MΩ cm) was got by water purification system (Millipore, Bedford, MA,

USA).

Morphologies and sizes were characterized by a JEOL/JSM-7610Fplus scanning electron microscope (SEM, JEOL, Japan) with an accelerating voltage of 15 kV. X-ray photoelectron spectroscopy (XPS) was obtained with K-Alpha (Thermo Fisher Scientific, USA). Powder X-ray diffraction (PXRD) was performed on Empyrean (PANalytical, Netherlands). Brunauer-Emmett-Teller (BET) specific surface area and pore volume were tested by N_2 adsorption-desorption experiments on Kubo X1000 (Beijing BUILDER electronic technology CO., Ltd, China). Ultraviolet-visible-near infrared (UV–vis–NIR) absorption spectra were conducted on UV-2600 UV-vis spectrophotometer (Shimadzu, Japan). Fourier transform infrared (FT-IR) spectra were measured by Spectrum Two (PerkinElmer Ltd., USA). Fluorescent spectra were recorded by a LS-55 spectrofluorometer (PerkinElmer Ltd., USA) with a voltage of 700 V and slit width of 10 nm for excitation and emission. Humidified incubator (Thermo Forma 3111, Thermo Fisher Scientific, Inc.) was selected for incubation. Samples were centrifuged by a TG 16-WS centrifuge (Hunan Cenlee Scientific Instrument Co. Ltd., China) and dried through a Taisite WGL-30D drying oven (Taisite, China). The diode laser was supplied by LSR808NL-2W-FC (Lasever, China). The thermal images were captured by an infrared thermal imager (Magnity D f10F1 A1 F) and processed in ThermoX software (Magnity technologies, China). Electrochemical detections were measured in CHI 660E electrochemical workstation (CH Instrument, USA). Hand-held homogenizer (S10, TUOHE, China) was used for real samples pretreatment. The HPLC analysis was conducted on an Agilent 1260 HPLC system (Agilent Technologies, Santa Clara, CA) with a Waters Symmetry C_{18} chromatographic column (250 nm × 4.6 mm i.d., 5 µm, Waters, Milford, MA). Bruker compact QTOF-MS system with electrospray ionization ion source was used for MS data acquisition (Bruker, Germany). The

parameters in positive ion mode were set as follows: scan range, m/z 50–1000; spray voltage, 3.5 kV; flow rate of dry gas, 8.0 L min^{-1}; temperature, 200 °C; nebulizer pressure, 35 psi.

1.2. Synthesis of MOFs

Cu-BTC was prepared according to previously reported method with minor modification.[1] $CuSO_4 \cdot 5H_2O$ (5.368 g) was mixed with H_3BTC (2.5 g) in mixed solvent of DMF, ethanol, and deionized water (75 mL, 1:1:1, v/v), which was stirred for 30 min at room temperature and then transferred to a Teflon-lined stainless-steel reactor (100 mL) and reacted at 85 °C for 12 h. After centrifugation, the solid precipitate (Cu-BTC) was separated, washed successively with DMF and ethanol twice, and vacuum-dried overnight at 60 °C.

CuNi-BTC was synthesized in two steps.[2] Firstly, Ni-BTC was synthesized as follows. $Ni(NO_3)_2 \cdot 6H_2O$ (2.28 g) was added into a beaker with DMF (40 mL) and sonicated for 15 min. After that, H_3BTC (0.88 g) was added for complete dissolution, and then transferred to a Teflon-lined stainless-steel reactor (100 mL) for reaction at 150 °C for 24 h. Ni-BTC was centrifuged for separation, washed with DMF and methanol three times, and dried overnight at 80 °C. Subsequently, Cu $(NO_3)_2 \cdot 3H_2O$ (0.40 g) was dissolved in methanol (20 mL), and then Ni-BTC (1.0 g) was added with sufficient stirring for 24 h at room temperature. Finally, CuNi-BTC was washed with methanol 3 times and dried overnight at 80 °C.

CuNi-BDC was synthesized according to previously reported solvothermal method.[3] Briefly, $Ni(NO_3)_2 \cdot 6H_2O$ (0.30 g) and $Cu(NO_3)_2 \cdot 3H_2O$ (0.145 g) were dissolved in DMF (20 mL), and simultaneously BDC (0.154 g) was added into DMF (10 mL). Two solutions were mixed and stirred for 10 min. After that, NaOH (0.2 g mL^{-1}, 2 mL) solution was dropped, and the mixture was reacted in an autoclave at 120

°C for 16 h. CuNi-BDC was obtained by washing the precipitate with ethanol and dried overnight at 150 °C.

CuNi-HATP was prepared according to the literature.[4] $Ni(CH_3COO)_2 \cdot 4H_2O$ (92.9 mg) and $Cu(NO_3)_2 \cdot 3H_2O$ (45.1 mg) were dissolved in deionized water (5 mL), and then under stirring, $NH_3 \cdot H_2O$ (6 mL) was added dropwise. The mixtures were then mixed with HATP·6HCl aqueous solution (20 mg mL^{-1}, 10 mL) and stirred at 65 °C for 2 h. CuNi-HATP was finally retrieved *via* centrifugation, washed with water and acetone three times, dried overnight at 60 °C.

The amount of Cu^{2+} and Ni^{2+} contents was measured by inductively coupled plasma optical emission spectrometer (ICP-OES, IICP-7700, Ewai, China).

1.3. Cyclic Voltammetry Experiment

A three-electrode system, consisting of a Pt wire (counter electrode), an Ag/AgCl (reference electrode), and a modified glass carbon electrode (GCE, working electrode), was selected to conduct electrochemical tests.[5] GCE was polished with α-Al_2O_3 powder (0.05 μm) and ultrasonically cleaned in water and ethanol. $NaNO_3$ (0.1 mol L^{-1}) aqueous solution was selected as electrolyte. Sample solution (10 μL, 2 mg mL^{-1}) containing 0.5% Nafion film was dropped on the surface of GCE and dried under infrared lamp. The scan rate was set as 100 mV s^{-1} and the potential range was set between −1 V and +1.5 V. Electrochemical impedance spectroscopy (EIS) test was conducted at the frequency of 0.1 Hz–1.0 MHz.

1.4. Calculation of Photothermal Conversion Efficiency

Sample was irradiated by NIR laser (808 nm, 2.0 W cm^{-2}) for a duration of 8 min to reach equilibrium, whereas temperature signals were acquired in real-time with a thermal imaging camera. Subsequently, the laser was switched off to naturally cool the solution to room temperature. During the cooling process, the temperature was recorded

every 60 s. Then photothermal conversion efficiency (η) was calculated by equation (1):[6]

$$\eta = \frac{mc(T_{max} - T_{max,H2O})}{I(1 - 10^{-A})\tau_s}$$

(1)

wherein A is the absorbance of material dispersion at 808 nm, m is the mass, c is the heat capacity of water (4.2 J g^{-1} K^{-1}), I is the power of laser (2.0 W cm^{-2}), $T_{max,H2O}$ and T_{max} are the maximum temperature values of H_2O and material system, and τ_s is the constant number for the material being calculated by equation 2:[6]

$$t = -\tau_s \cdot \ln\left(\frac{T - T_{surr}}{T_{max} - T_{surr}}\right) = -\tau_s \cdot \ln(\theta)$$

(2)

wherein t is the time responding to the real-time temperature (T) change of material dispersion, T_{surr} is the temperature of the surrounding environment, which equals to 20.0 °C. Finally, τ_s can be calculated according to the linear regression of the cooling profile.

1.5. Theoretical Calculation

Time-dependent density functional theory (TD-DFT) calculations were used for the theoretical investigation of ESIPT mechanism. Local minima and transition state structures were obtained by optimization of geometry. Geometries were determined with the B3LYP/6-31+G (d) basis set, while energies were determined by single point calculations with the B3LYP/6-311+G (d,p) basis set upon optimized structures. All calculations were performed using GaussView 5.0 package.

1.6. Calculation of Optical Band Gap Energy

Optical band gap energy (Eg) was calculated by equation 3:[7]

$$(\alpha h v)^r = A(h v - Eg)$$

(3)

Wherein α, h, v, A and Eg are the absorption coefficient, Planck constant, light

frequency, proportionality constant, and band gap, and $r = 0.5$ and 2 are for a direct band gap material and an indirect band gap material.

1.7. CuNi-BTC Catalytic Oxidation and Polymerization of *o*-Phenylenediamine

CuNi-BTC aqueous dispersion (39 mg L^{-1}, 100 μL), OPD aqueous solution (120 mM, 100 μL), and Tris-HCl buffer (pH 8.5, 10 mM, 100 μL) were mixed in a centrifuge tube (0.5 mL). Mixtures were incubated at 37 °C, and UV–vis–NIR absorption spectra at different incubation time were collected. After incubation for 60 min, the solution was irradiated by NIR laser (808 nm, 2.0 W cm^{-2}) for a duration of 8 min to reach equilibrium, whereas the IR thermal images and temperature signals were acquired and analyzed with a thermal imaging camera. In addition, the oxidation products were separated by centrifugation. The precipitate was washed by deionized water three times, and dried at 40 °C overnight under vacuum for characterization.

1.8. Specific detection of Thiophanate-methyl by Photothermal Method

TM solutions (50 μL) with different concentrations were mixed with CuNi-BTC solution (39 mg L^{-1}, 50 μL) and incubated at 37 °C for 40 min to inhibit the catalytic activity of CuNi-BTC. Then, OPD aqueous solution (120 mM, 100 μL) and Tris-HCl buffer (pH 8.5, 10 mM, 100 μL) were added and incubated at 37 °C for another 60 min in the dark. Finally, the resulting solutions were irradiated by NIR laser (808 nm, 2.0 W cm^{-2}) for 8 min and the thermal images of the reaction system were monitored by a thermal imaging camera. All measurements were carried out in triplicate.

1.9. Detection of Thiophanate-methyl in real samples

Fresh food samples (pakchoi and apple) were got from local supermarket (Changsha, China) and used to evaluate the feasibility in practical applications. Food samples were pretreated according to our previously reported method.[5] In brief, food samples (100.0 g) were sprayed with different concentrations of TM, chopped,

homogenized, extracted with ultrasonic in acetonitrile (10 mL, 10 min), and then centrifuged at 5000 rpm for 2 min. Thereafter, the supernatant was filtered with a 0.22 μm membrane and stored at 4 °C. For real sample analysis, sample solution (50 μL) was subjected to photothermal testing by the operation procedures as described above. The spiked amounts were calculated according to the standard curve method. Three parallel experiments were carried out for each sample to obtain the relative standard deviation. What is more, high performance liquid chromatography (HPLC) of each sample was conducted to verify the reliability of the fabricated photothermal method.

1.10. Analysis of TM by HPLC

HPLC analysis was conducted using an Agilent 1260 HPLC system (Agilent Technologies, Santa Clara, CA). A Waters Symmetry C_{18} chromatographic column (250 nm × 4.6 mm i.d., 5 μm, Waters, Milford, MA) was selected for analysis. The mobile phase consisted of 0.1% (v/v) formic acid solution (A) and acetonitrile (B) with a gradient elution mode (0–7 min, 50–85% B) at 25 °C. The flow rate and injection sample volume were 1.0 mL min^{-1} and 20 μL. The chromatogram was acquired at 285 nm.
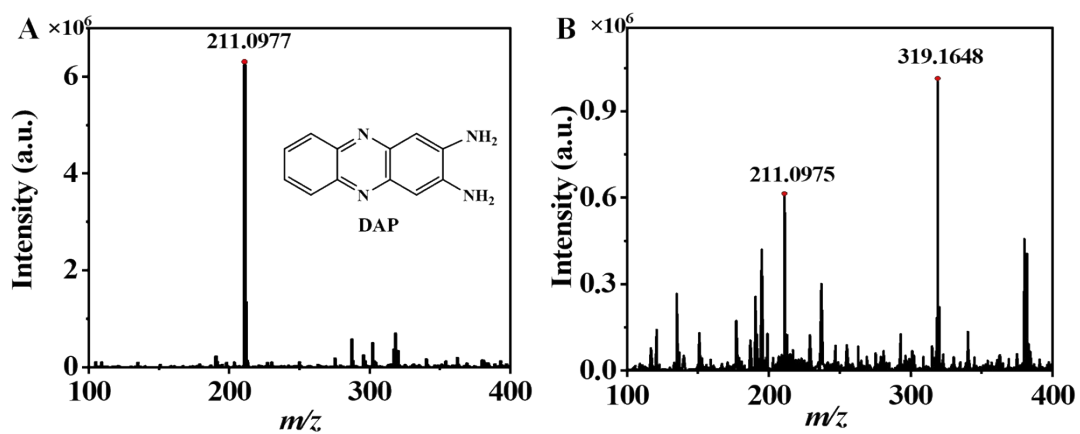
Fig. S1 Structure characterization of oxidized OPD. Mass spectrometry of product for Cu^{2+} + OPD (A) and Cu^{2+} + Ni^{2+} + OPD (B) reaction system.

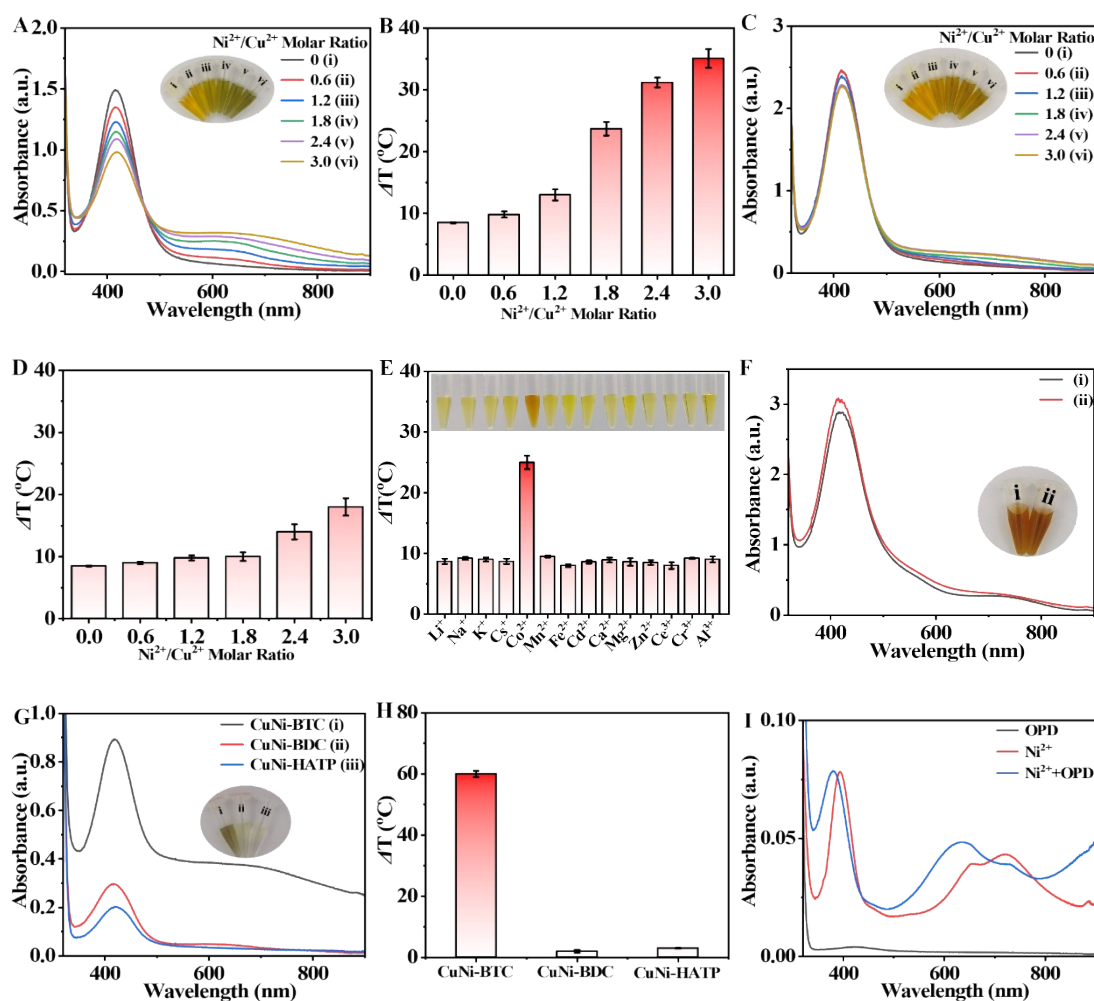**Fig. S2** Effect of metal ions and MOFs on OPD reaction. UV−vis−NIR spectra (A) and ΔT (B) change of Ni^{2+} + Cu^{2+} + OPD systems; UV−vis−NIR spectra (C) and ΔT (D) change of Ni^{2+} addition to the completed Cu^{2+} + OPD solution; (E) ΔT for metal ions (30 μM) + Cu^{2+} + OPD reaction systems; (F) UV−vis−NIR spectra of Co^{2+} (30 μM) + Cu^{2+} + OPD (i) and Co^{2+} addition to the completed Cu^{2+} + OPD solution. The introduction of Co^{2+} results in the orange-red color solution and the temperature change at 25 °C. Two absorption peaks at 570 (sh) and 740 nm might come from the chelating between Co^{2+} and DAP; UV−vis−NIR spectra (G) and ΔT (H) of reaction products in CuNi-BTC/CuNi-BDC/CuNi-HATP (13 mg L^{-1}) + OPD (40 mM) systems; UV−vis−NIR spectrum (I) of Ni^{2+} (3 mM) and OPD systems. Concentrations for Cu^{2+} and OPD were 10 μM and 40 mM (insets: corresponding images under daylight).
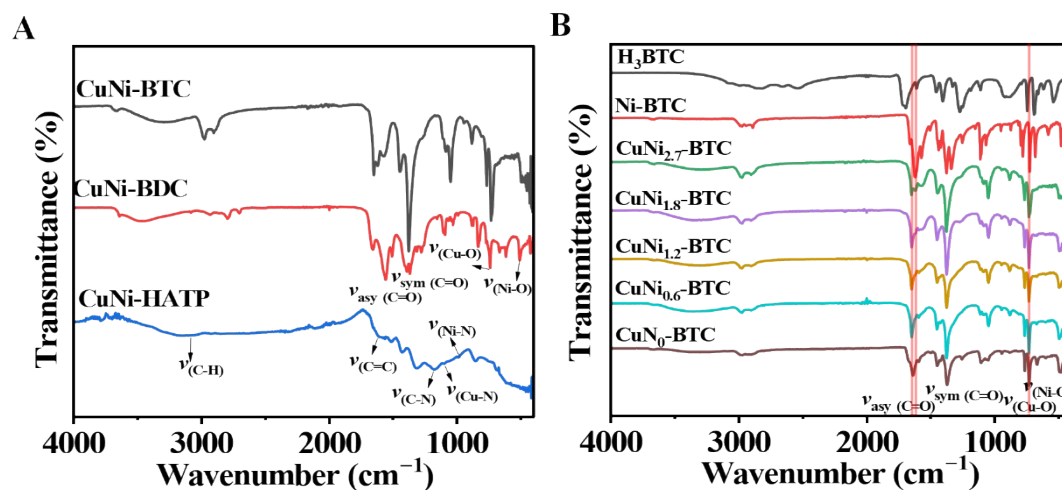
Fig. S3 Characterization of as-synthesized MOFs. FT-IR spectra of CuNi-BTC, CuNi-BDC, and CuNi-HATP (A); FT-IR spectra of H_3BTC, Ni-BTC, and CuNi$_x$-BTC (B).

By comparing the FT-IR spectrum of H_3BTC (1698 and 1405 cm^{-1} for asymmetric (ν_{asy}) and symmetric (ν_{sym}) C=O stretching vibrations), the $\nu_{asy(C=O)}$ peak shifts significantly to 1616 cm^{-1} in Ni-BTC and 1637 cm^{-1} in Cu-BTC due to the interaction between COO$^-$ and metal ions.[8] The Cu–O and Ni–O peaks are found at 722 and 454 cm^{-1}, respectively.[9] As the concentration of Cu^{2+} increases, the peak at 1616 cm^{-1} fades away while the peak at 1637 cm^{-1} enhances gradually. Similar characteristic stretching vibrations were found for CuNi-BDC. For CuNi-HATP, the vibration peak at 1173 cm^{-1} derives from the C–N group, whereas the Cu–N and Ni–N peaks are observed at 1094 and 977 cm^{-1}, indicating the successful synthesis of CuNi-HATP.[10] All above characteristic peaks indicate that Cu^{2+} and Ni^{2+} have coordinated with BTC, BDC, and HATP successfully.
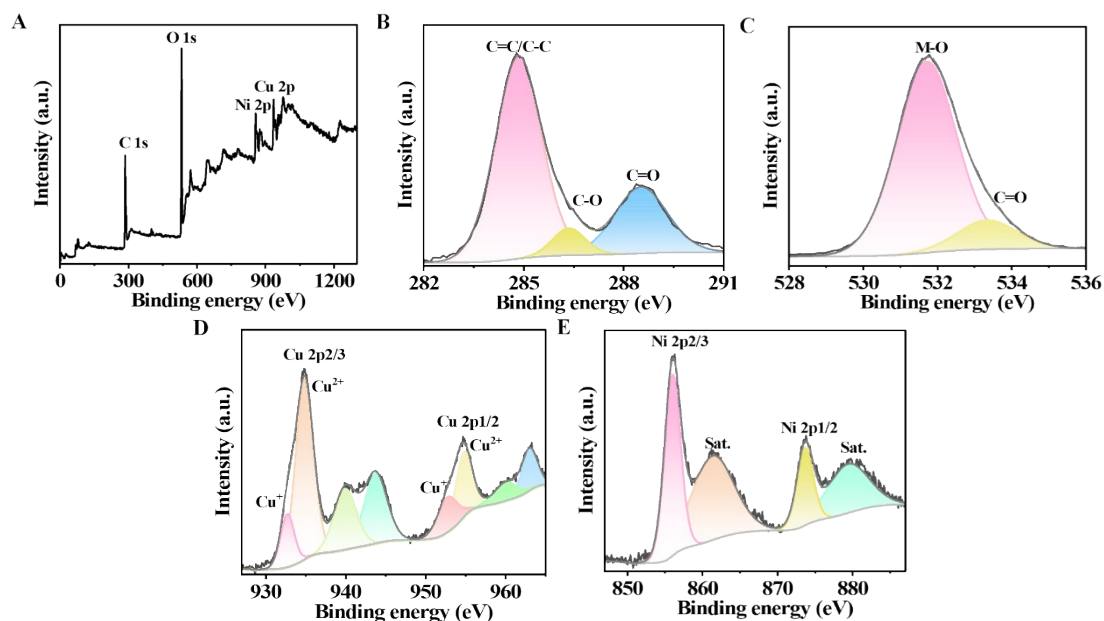
Fig. S4 Characterization of CuNi-BTC. Full XPS spectrum of CuNi-BTC (A), and the corresponding high resolution XPS spectra of C1s (B), O1s (C), Cu 2p (D), Ni 2p (E).

Full XPS spectrum of CuNi-BTC indicates the presence of C, O, Cu, and Ni. Three peaks appear at binding energies of 284.8, 286.4, and 288.6 eV in high-resolution C1s spectrum, which belong to the C=C/C–C, C–O and C=O groups.[3,11] As shown in O1s XPS spectrum, two dominant peaks at 531.8 and 533.4 eV are related to the M–O groups (M=Cu, Ni) and C=O.[12] In the core-level Cu 2p spectrum, the spin-orbit and satellite peaks of Cu 2p3/2 and Cu 2p1/2 are observed at 934.8, 943.8, 954.9, and 963.1 eV, indicating the existence of Cu^{2+} in the CuNi BTC. The lower binding energy of 932.8 eV (2p 3/2) and 953.0 eV (2p 1/2) demonstrate the existence of Cu^{+}.[13] The characteristic Ni 2p3/2 and Ni 2p1/2 peaks are respectively located at 856.1 and 873.7 eV in the core-level Ni 2p spectrum with the spin−orbit energy difference of 17.6 eV, related to the presence of Ni^{2+} in CuNi BTC.[14] The satellite peaks correlated to Ni 2p3/2 and Ni 2p1/2 peaks are exhibited at 861.5 and 879.7 eV, respectively.
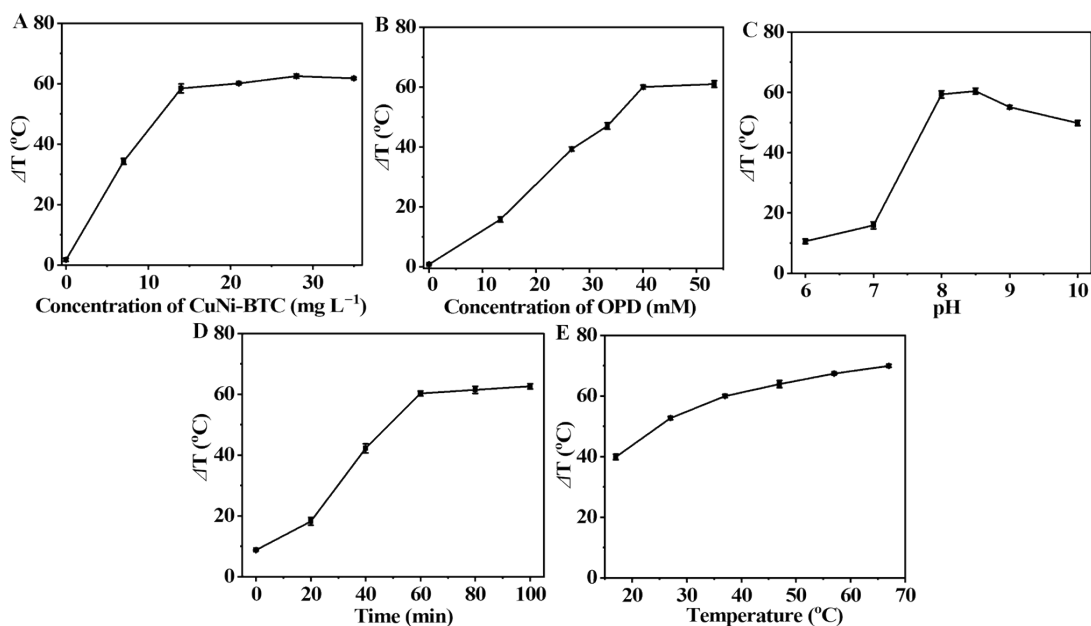
Fig. S5 Optimization of CuNi-BTC + OPD reaction system. ΔT (^{o}C) of CuNi-BTC + OPD reaction system with different Ni^{2+}/Cu^{2+} molar ratios (A), CuNi-BTC concentration (B), OPD concentration (C), pH (D), reaction time (E), and reaction temperature (F).
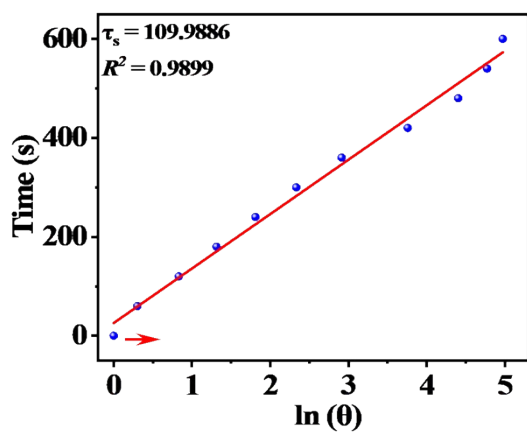

Fig. S6 Plot of linear time data from the cooling stage of CuNi-BTC + OPD system versus negative natural logarithm of the drive force temperature. The slope represents the sample system time constant (τs).
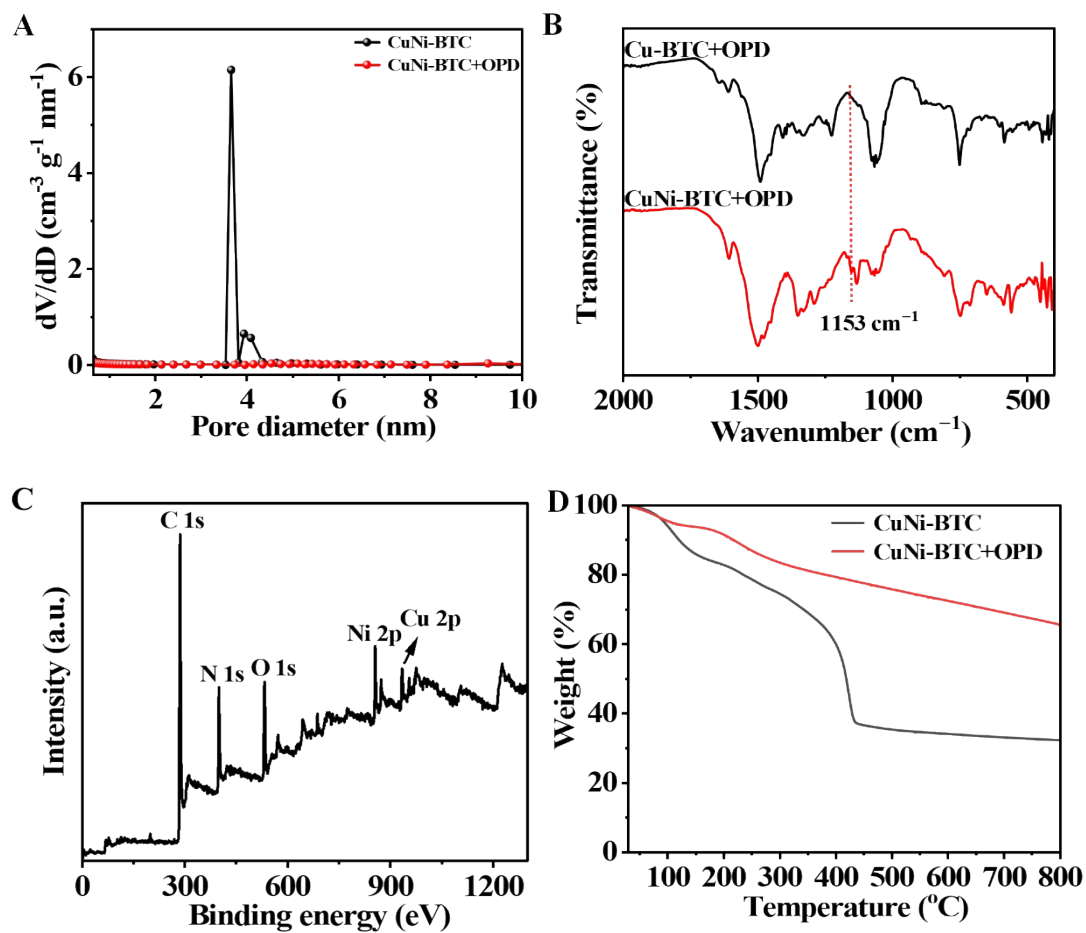
Fig. S7 Characterization of CuNi-BTC and CuNi-BTC + OPD. Pore size distribution curves (A), FT-IR spectra (B), and thermogravimetric analysis curves (D) of CuNi-BTC and CuNi-BTC + OPD; The full XPS spectrum of CuNi-BTC + OPD (C).
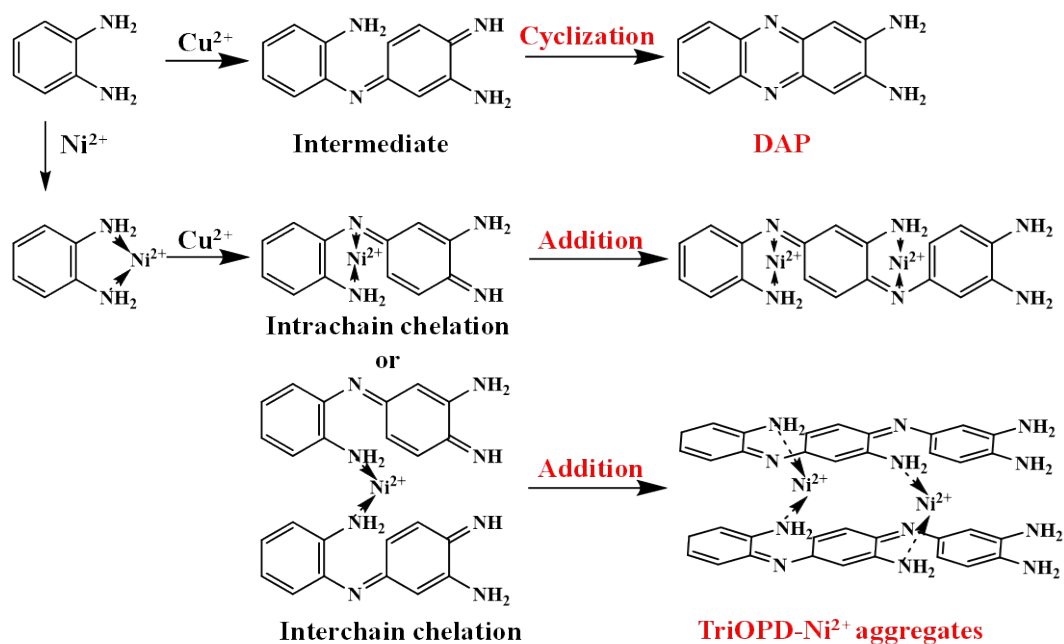
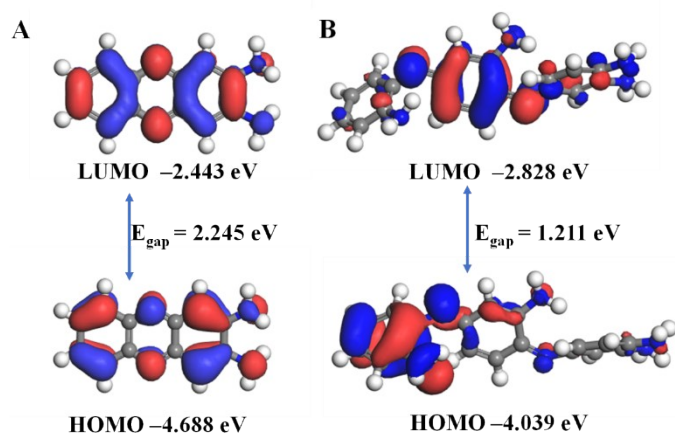**Fig. S8** Possible reaction pathways for Ni^{2+} mediated Cu^{2+} oxidation, polymerization, and aggregation of OPD.

Fig. S9 Density functional theory calculations. The highest occupied molecular orbital (HOMO) and lowest unoccupied molecular orbital (LUMO) diagrams of DAP (A) and triOPD (B).
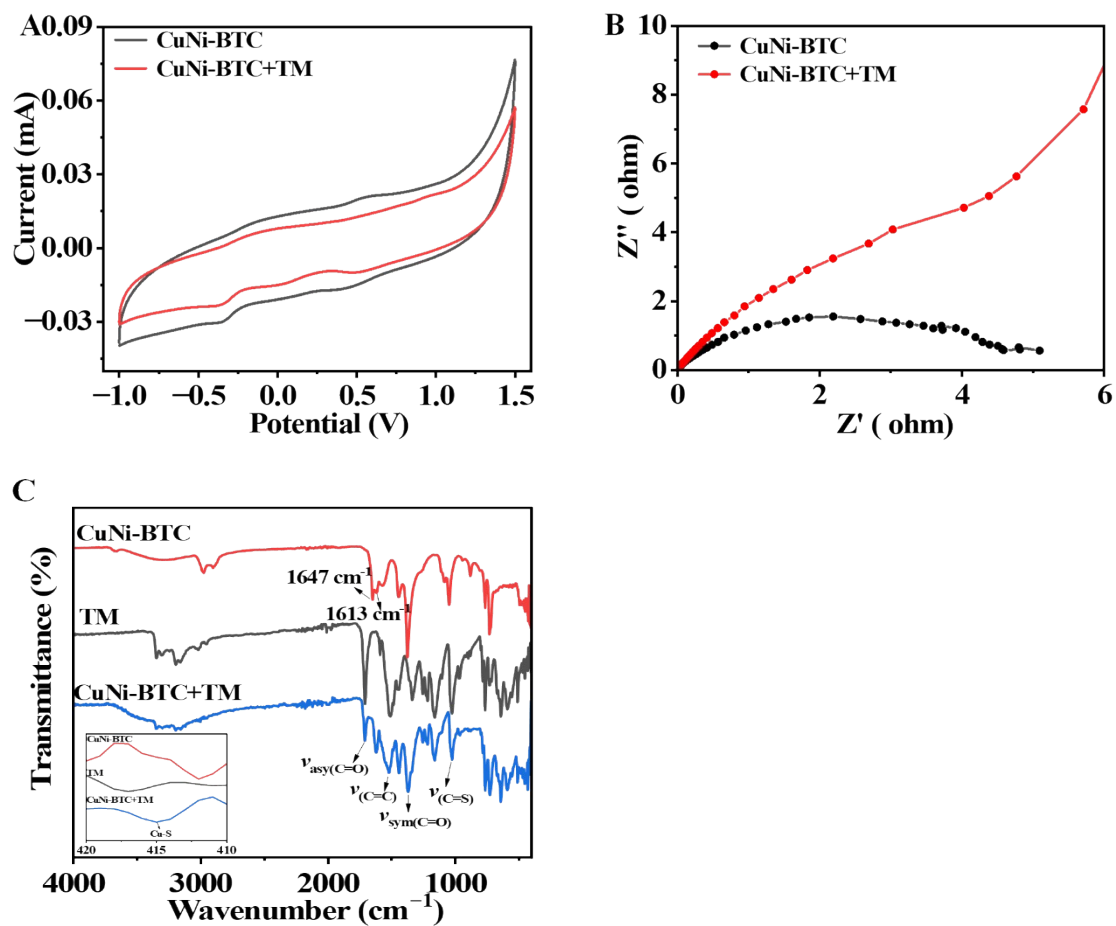
Fig. S10 Detection mechanism of TM. Cyclic voltammograms (A) and electrochemical impedance spectroscopy curves (B) for CuNi-BTC and CuNi-BTC + TM; (C) FT-IR spectra of CuNi-BTC, TM and CuNi-BTC + TM.
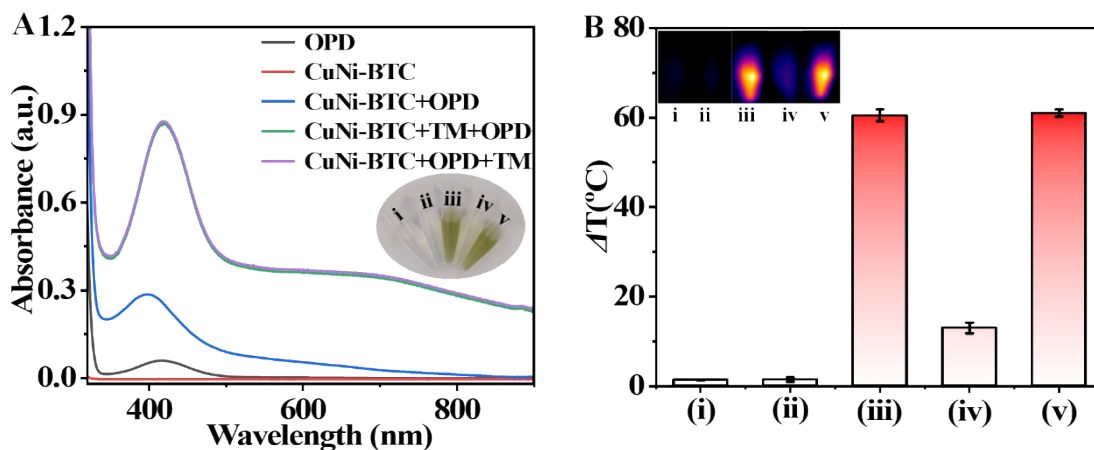
Fig. S11 Detection mechanism of TM. (A) UV−vis−NIR spectra and ΔT (B) for reaction systems of OPD (40 mM) (i), CuNi-BTC (13 mg L^{-1}) (ii), CuNi-BTC (13 mg L^{-1}) + OPD (40 mM) (iii), and CuNi-BTC (13 mg L^{-1}) firstly incubation with TM (7.5 µM) followed by addition with OPD (40 mM) (iv); TM (7.5 µM) addition into CuNi-BTC (13 mg L^{-1}) + OPD (40 mM) reaction system (iv) (insets: corresponding images under daylight and thermal camera).
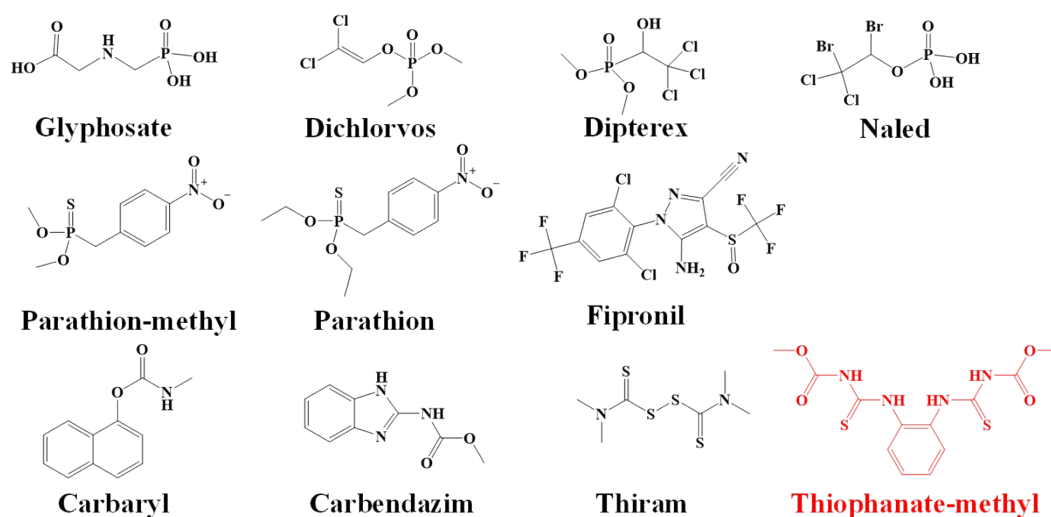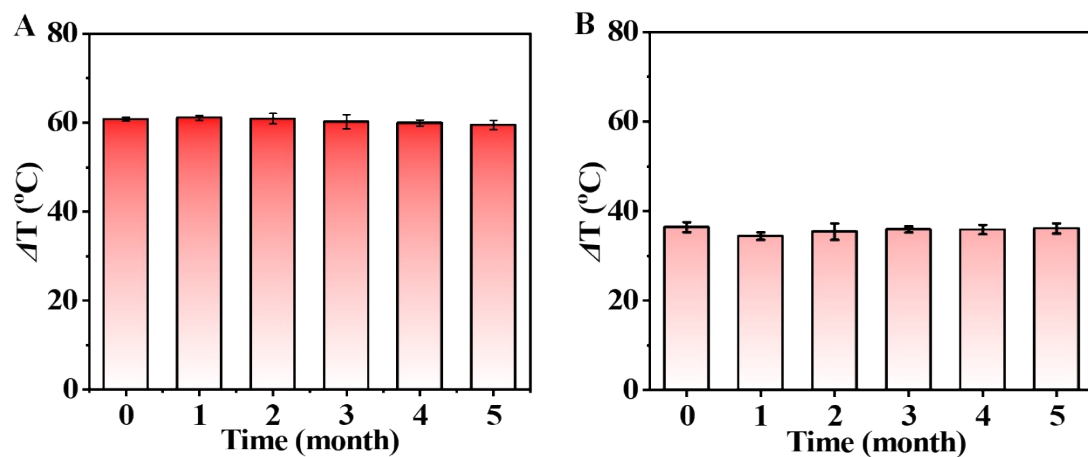

Fig. S12 Pesticides used in experiments.

Fig. S13 Storage stability of CuNi-BTC. $\varDelta$T for (A) CuNi-BTC (13 mg L^{-1}) + OPD (40 mM) and (B) CuNi-BTC (13 mg L^{-1}) + TM (7.5 μM) + OPD (40 mM) with different storage time for CuNi-BTC.
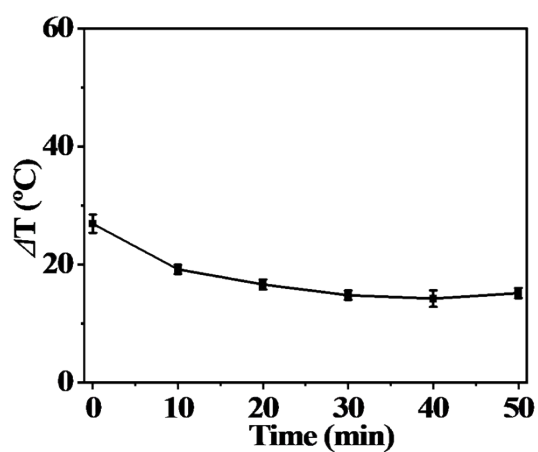

Fig. S14 Optimization of reaction time for TM. $\varDelta$T (°C) of CuNi-BTC (13 mg L^{-1}) and TM (7.5 μM) incubation at different time and then addition of OPD (40 mM) for 60 min reaction.
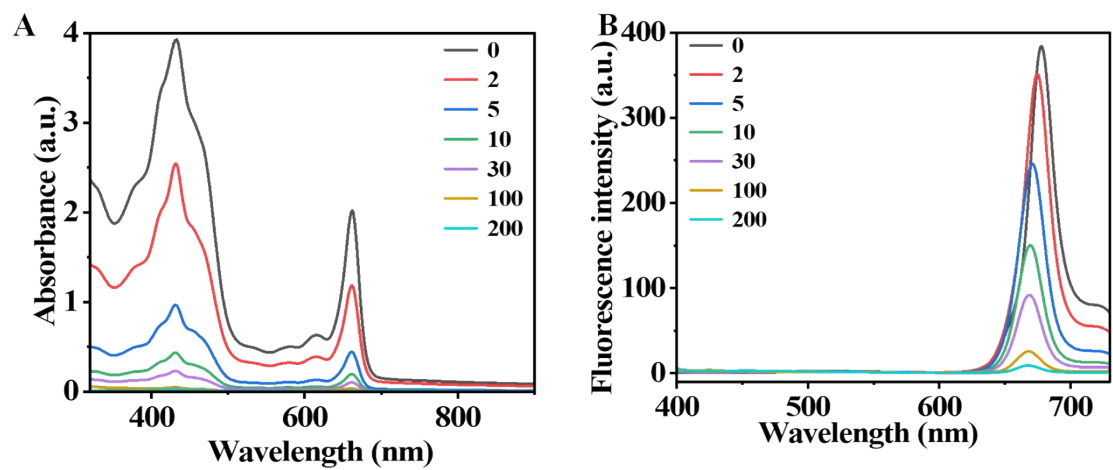
Fig. S15 UV−vis−NIR (A) spectra, and fluorescence spectra (B) of pakchoi extract solutions with different dilution ratios.

Table S1

Comparison of the proposed sensing in this work with reported methods for TM

Method	Probes[a]	Linear range (μM)	LOD (μM)	References
Surface-enhanced Raman spectroscopy	$Fe_3O_4@SiO_2@Ag$-SH	0.3–1.8	0.2	15
Colorimetry	Cu@NC	0.6–43	0.11	16
Colorimetry	Ce-GONRs	0.3–14.6	0.2	17
Fluorometry	CuI-p-DPA	0.5–100	0.01	18
Fluorometry	CDs@Cu-MOFs	0.03–0.8	0.004	19
Fluorometry	SCDs	0.05–5	0.0076	20
Fluorometry	CDs	0–10	0.05	21
Photothermal	CuNi-BTC+OPD	0.5–7.5	0.05	This work

detection.

[a]Cu@NC, Cu-doped carbon nanozyme; Ce-GONRs, nanoceria crosslinked graphene oxide nanoribbons; CuI-p-DPA, copper iodide coordination dopamine polymer; SCDs, thioctic acid-carbon dots.

Table S2.

Detection of TM in spiked samples by the proposed photothermal method and HPLC.

Sample	Spiked (μg kg⁻¹)	Found (μg kg⁻¹)	Recovery (%)	RSD (%)	HPLC (μg kg⁻¹)	Recovery (%)	RSD (%)	Relative error (%)
Pakchoi	0	–	0	–	–	0	–	–
	34.2	34.6 ± 1.94	101.3	5.7	33.9 ± 0.07	99.3	0.2	1.3
	85.5	85.8 ± 3.37	105.5	4.9	84.9 ± 0.27	98.9	0.3	1.0
	170.0	166.3 ± 0.78	97.8	0.5	172.5 ± 0.24	101.5	0.2	2.5
Apple	0	–	0	–	–	0	–	–
	34.2	36.2 ± 2.14	105.8	6.2	35.7 ± 0.28	104.5	0.8	0.8
	85.5	79.5 ± 3.92	93.0	4.6	86.2 ± 0.34	100.8	0.4	5.5
	170.0	165.6 ± 2.43	97.4	1.4	167.9 ± 0.6	98.8	0.4	0.9

References

1 S. Li, Z. Wei, L. Xiong, Q. Xu, L. Yu, Y. Xiao, *Anal. Chem.*, 2022, **94**, 17263–17271.

2 W. Zou, H. Li, M. Liu, Y. Lv, *Appl. Catal. A: Gen.*, 2023, **656**, 119120.

3 S. Rajasekaran, B. S. Reghunath, K. R. Sunaja Devi, D. Pinheiro, *Mater. Today Chem.*, 2023, **31**, 101616.

4 J. Yan, J. Li, P. Liu, H. Huang, W. Song, *Green Chem.*, 2023, **25**, 8645.

5 Y. Yang, J. Xu, R. Zhou, Z. Qin, C. Liao, S. Shi, Y. Chen, Y. Guo, S. Zhang, *Carbon*, 2024, **219**, 118831.

6 X. Li, L. Yang, C. Men, Y. F. Xie, J. J. Liu, H. Y. Zou, Y. F. Li, L. Zhan, C. Z. Huang, *Anal. Chem.*, 2019, **91**, 4444–4450.

7 Q. Hou, C. Xue, N. Li, H. Wang, Q. Chang, H. Liu, J. Yang, S. Hu, *Carbon*, 2019, **149**, 556–563.

8 G. Guo, *J. Mater. Sci.: Mater. Electron.*, 2021, **32**, 16287–16301.

9 V. Archana, Y. Xia, R. Fang, G. G. kumar, *ACS Sustainable Chem. Eng.*, 2019, **7**, 6707−6719.

10 B. Tian, S. Liu, L. Feng, S. Liu, S. Gai, Y. Dai, L. Xie, B. Liu, P. Yang, Y. Zhao, *Adv. Funct. Mater.*, 2021, **31**, 2100549.

11 Y. Shu, L. Yan, M. Ye, L. Chen, Q. Xu, X. Hu, *Analyst*, 2023, **148**, 4721.

12 S. N. Shreyanka, J. Theerthagiri, S. J. Lee, Y. Yu, M. Y. Choi, *Chem. Eng. J.*, 2022, **446**, 137045.

13 J. Wang, R. Huang, W. Qi, R. Su, Z. He, *Chem. Eng. J.*, 2022, **434**, 134677.

14 Y. Zhang, T. Luan, Q. Fang, Z. Song, X. Shang, L. Lu, Y. Du, *Sens. Actuator. B Chem.*, 2024, **401**, 135068.

15 T. Wang, C. Xie, Q. You, X. Tian, X. Xu, *Food Chem.*, 2023, **424**, 136479.

16 M. Zhang, Y. Wang, N. Li, D. Zhu, F. Li, *Biosens. Bioelectron.*, 2023, **237**, 115554.

17 S. Tai, J. Wang, F. Sun, Q. Pan, C. Peng, Z. Wang, *Anal. Chim. Acta*, 2023, **1283**, 341929.

18 Q. Zhou. H. Zhao, D. Chen, H. Sun, K. Zhang, C. Wang, Q. Cao, L. Zheng, *Analyst*, 2023, **148**, 5889.

19 Y. Yu, G. Huang, X. Luo, W. Lin, Y. Han, J. Huang, Z. Li, *Microchim. Acta*, 2022, **189**, 325.

20 S. Wang, H. Chen, H. Xie, L. Wei, L. Xu, L. Zhang, W. Lan, C. Zhou, Y. She, H. Fu, *Food Chem.*, 2021, **346**, 128923.

21 Y. Wang, Y. Ma, H. Wan, F. Shang, B. Yang, Y. Han, *Food Chem.*, 2024, **441**, 138413.